Opto-Electronic Advances

Original Article

2018, Vol. 1, No. 7

DOI: 10.29026/oea.2018.180003

Fiber-based mode converter for generating optical vortex beams

Ruishan Chen[1†], Jinghao Wang[1†], Xiaoqiang Zhang[1,2], Junna Yao[1], Hai Ming[1] and Anting Wang[1*]

In this work, an all-fiber-based mode converter for generating orbital angular momentum (OAM) beams is proposed and numerically investigated. Its structure is constructed by cascading a mode selective coupler (MSC) and an inner elliptical cladding fiber (IECF). OAM modes refer to a combination of two orthogonal LP_{lm} modes with a phase difference of ±π/2. By adjusting the parameters and controlling the splicing angle of MSC and IECF appropriately, higher-order OAM modes with topological charges of l = ±1, ±2, ±3 can be obtained with the injection of the fundamental mode LP_{01}, resulting in a mode-conversion efficiency of almost 100%. This achievement may pave the way towards the realization of a compact, all-fiber, and high-efficiency device for increasing the transmission capacity and spectral efficiency in optical communication systems with OAM mode multiplexing.

Keywords: optical vortices; fiber optics; singular optics; mode-division multiplexing

Chen R S, Wang J H, Zhang X Q, Yao J N, Ming H *et al*. Fiber-based mode converter for generating optical vortex beams. *Opto-Electronic Advances* **1**, 180003 (2018).

Introduction

Optical vortex beams (OVBs) possessing orbital angular momentum (OAM), i.e., OAM beams or OAM modes, with a helical phase wavefront indicated by the term $\exp(il\varphi)$, where φ denotes the azimuth angle and l is an integer representing topological charges (TCs), have a phase singularity in the transverse phase center and a doughnut-shaped profile in the transverse intensity distribution[1].

In recent decades, mode-division multiplexing has increasingly attracted attention as a method for increasing the transmission capacity and spectral efficiency of optical communication systems, with a special focus on multiplexing technology with OAM modes because of their infinite value of $l\hbar$ per photon[2–4]. In addition, OAM beams have been developed for applications such as optical tweezers and atom manipulation[5–7], microscopy[8], as well as quantum information processing[9].

A pivotal challenge is the generation of OAM beams, for which various methods have been developed. Free-space optical systems, such as spiral phase plates[10], cylindrical lens converters[11], and spatial light modulators (SLM)[7–9], are relatively bulky or expensive. Hence, various fiber-based generation schemes have been investigated, such as acoustic-optic interaction[12], mechanical stress-induced long-period grating[13,14], CO_2 laser-inscribed long-period fiber grating[15], offset splicing[16] or pressure exertion[17] in a single-ring fiber, and the superposition of two orthogonal LP_{11} modes with a micro phase difference, because of their superior robustness, low cost, compatibility, and high efficiency. In these previous papers, however, only OAM modes for l = ±1 have been achieved, which makes the development of high-capacity all-fiber communication systems based on OAM modes difficult. Therefore, it is highly desirable to generate high-order OAM (HO-OAM) modes. In our previous work, we theoretically studied the generation of first-order OAM modes[18] and HO-OAM modes by using a helical fiber Bragg grating[19]. Moreover, Fang *et al*. simulated the flexible generation of HO-OAM modes by using helical long-period fiber gratings[20–21]. Furthermore, theo-

[1]Department of Optics and Optical Engineering, University of Science and Technology of China, Hefei 230026, China; [2]Hefei General Machinery Research Institute, Hefei 230031, China

† These authors contributed equally to this work.

* Correspondence: A T Wang, E-mail: atwang@ustc.edu.cn

Received 7 February 2018; accepted 9 April 2018; accepted article preview online 13 August 2018

retical methods for generating HO-OAM modes were proposed by phase-matching coupling between different vector modes[22–24]. In addition, integrated photonics-based methods have been implemented for OAM multiplexing and generation, which realize relatively compact systems[25–31].

In this letter, an all-fiber-based mode converter for the efficient generation of OAM modes with TCs of l = ±1, ±2, ±3 is proposed and simulated in detail. The mode converter is developed by combining a mode-selective coupler (MSC)[32] and an inner elliptical cladding fiber (IECF). The MSC is used to generate LP_{lm} modes, where l denotes the azimuthal index and m represents the radial index, which is assumed as 1, and the IECF can introduce a phase difference of ±π/2 between two degenerate orthogonal (LP_{l1}^{even} and LP_{l1}^{odd}) modes after a certain propagation length. Consequently, the HO-OAM modes can be obtained with a high mode-conversion efficiency of close to 100%.

Mode-selective coupler

As a part of the proposed mode converter, the MSC is composed of a single-mode fiber (SMF) and a multimode fiber (MMF), which has been exploited to excite the high-order modes (HOM) LP_{l1} in MMF with high efficiency[33]. The MSC has been used to generate OAM beams[34–35]. If the refractive-index difference between the core and cladding is small enough to satisfy the weak guiding approximation, the linearly polarized (LP) mode can be applied in the fiber. Based on the coupled-mode theory, the principle of MSC is to reach the phase-matching condition between the fundamental mode LP_{01} in the SMF and HOM LP_{l1} in the MMF. If the effective indices or propagation constants are equal, the phase-matching condition can be satisfied and the power of the LP_{01} mode in the SMF can be completely transferred to the LP_{l1} mode in the MMF with fiber lengths that are odd multiples of the half beat coupling length. For an MSC composed of two dissimilar fibers, the output power in the MMF can be expressed as[36]

$$P_c = \frac{P_0}{1+(\kappa\delta)^2}\sin^2(\sqrt{\kappa^2+\delta^2}\cdot L)\,, \tag{1}$$

where P_c is the optical power of the HOM in the MMF; P_0 is the optical power of the fundamental mode in the SMF; $\delta = (\beta_1-\beta_2)/2$ is the phase-mismatch factor; β_1 and β_2 are the propagation constants of the normal mode in the SMF and MMF, which are both equal to $2\pi\times n_{\text{eff}}/\lambda$; n_{eff} is the effective index; L is the coupling length; and κ is the coupling coefficient. The coupling coefficient can be expressed as[32]

$$\kappa = (-1)^l \frac{2\sqrt{2}k\rho_2\Delta_2 u_1 u_2 n_{\text{co}}}{\rho_1 v_1 v_2^3} \times \frac{K_l(\omega_1 d/\rho_1)}{K_1(\omega_1)\sqrt{K_{l-1}(\omega_2)K_{l+1}(\omega_2)}}\cos(l\alpha) \tag{2}$$

where u_1 and u_2 are the core modal indices of the SMF and MMF, respectively; ω_1 and ω_2 are the cladding modal indices of the SMF and MMF, respectively; v_1 and v_2 are the normalized frequencies of the SMF and MMF, respectively; l is the mode order in the azimuthal direction; k is the wave number; ρ_1 and ρ_2 are the core radii of the SMF and MMF, respectively; Δ_2 is the relative index difference in the MMF; n_{co} is the fiber-core refractive index; d is the distance between the SMF and MMF for MSCs; K is the modified Bessel function of the second kind; and α is the azimuthal angle shown in Fig. 1 in Ref.[32].

It is assumed that the indices of the core and cladding are n_{co}=1.4392 and n_{cl} =1.431 for both the SMF and MMF, respectively; the distance between the SMF and MMF for MSCs is 18 μm; and the core radius of MMF is 9 μm. In order to completely transfer the power from the LP_{01} mode in the SMF to the LP_{l1} mode in the MMF, it is essential that the modes have the same n_{eff} or β. To achieve this, the SMF can be tapered to satisfy phase matching while the MMF has a constant diameter of 18 μm for easy cascading, as in Ref.[37]. In Fig. 1, the n_{eff} of the LP_{01} mode in the SMF as a function of the core radius (black curve) and those of the LP_{l1} modes in the MMF (horizontal color line) at a wavelength of λ =1550 nm are mapped. For realizing phase matching between the LP_{01} mode and the LP_{11}, LP_{21}, and LP_{31} modes, SMFs with different radii can be employed. Further, the radii of the SMFs of the MSCs (MSC_1, MSC_2, and MSC_3) are equal to 5 μm, 3.21 μm, and 1.98 μm, respectively, as shown in Fig. 1.

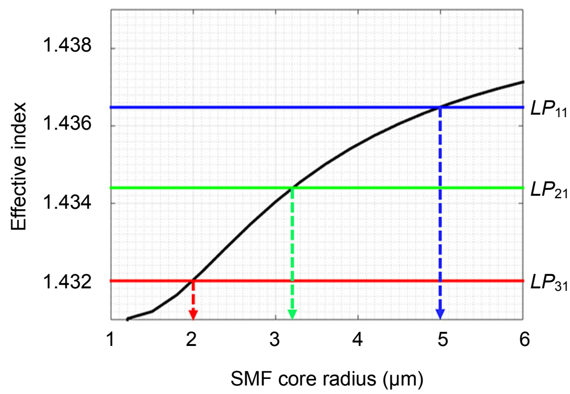

Fig. 1 | Effective indices of different modes in the SMF (LP_{01} mode) and MMF (LP_{l1} modes) at a wavelength of 1550 nm. The black curve shows the effective index of the fundamental mode in the SMF as a function of the core radius. The horizontal lines show the effective indices of the LP_{l1} modes in the MMF[32].

Based on the given parameters, we simulate the performance of MSCs. From the analysis in Ref.[32], the coupling coefficient between the LP_{01} mode and LP_{l1}^{s} mode (i.e., LP_{l1}^{s}=$F_{l1}(r)\sin(l\varphi)$, where $F_{l1}(r)$ is the radial wave function for LP_{l1} modes) is zero when the two cores of the MSC are in the same horizontal plane. Thus, if the input mode is the fundamental mode LP_{01} in the SMF,

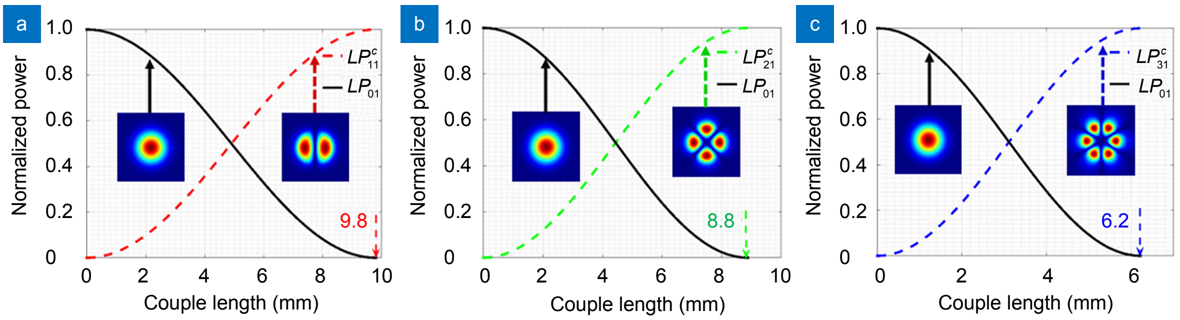

Fig. 2 | Normalized power conversion (a) from the LP_{01} mode to the LP_{11}^c mode in MSC$_1$, (b) from the LP_{01} mode to the LP_{21}^c mode in MSC$_2$, and (c) from the LP_{01} mode to the LP_{31}^c mode in MSC$_3$ between the SMF and MMF as a function of coupling length L. Insets: simulated intensity profiles of the LP_{01} and LP_{l1}^c modes.

only the LP_{l1}^c mode (i.e., $LP_{l1}^c = F_{l1}(r)\cos(l\varphi)$) can be selectively excited in the MMF. Figures 2(a)~2(c) show the normalized power conversion from the LP_{01} mode to the LP_{11}^c mode in MSC$_1$, from the LP_{01} mode to the LP_{21}^c mode in MSC$_2$, and from the LP_{01} mode to the LP_{31}^c mode in MSC$_3$, respectively. As the coupling length increases, the coupling power follows a sinusoidal oscillation. The coupling length L can be designed specifically to realize a maximum coupling efficiency of close to 100% for exciting the LP_{11}^c, LP_{21}^c, and LP_{31}^c modes in the MMF, and they are equal to 9.8 mm, 8.8 mm and 6.2 mm, respectively. The insets show the simulated intensity profiles of the LP_{01} and LP_{l1}^c modes.

Inner elliptical cladding fiber

Another critical part of the mode converter is the IECF, as shown in Fig. 3. Figure 3(a) shows the cross section and refractive-index distribution of the IECF, and Fig. 3(b) depicts the three-dimensional structure of the proposed IECF. The proposed fiber has two claddings, i.e., the inner elliptical cladding and outer circular-symmetry cladding. The elliptical cladding breaks circular symmetry, introduces birefringence, and removes the degeneracy of the fiber modes. The refractive indices of the outer cladding and inner core in the IECF are the same as those of the MMF in the MSC, which are equal to n_{oc}=1.431 and n_c= 1.4392, respectively. Furthermore, the refractive index of the inner elliptical cladding is set as n_{ic} =1.426. The lengths of the major and minor axis of the inner elliptical cladding are 60 μm and 18.6 μm, respectively. As shown in Fig. 3(b), the angle between the direction of the major axis of the ellipse and the vertical direction is θ, which should be set to $\pi/(4l)$ for the generation of LP_{l1} or HO-OAM modes[32,37]. In practice, the IECF can be fabricated by the standard MCVD method, as described in Ref.[38].

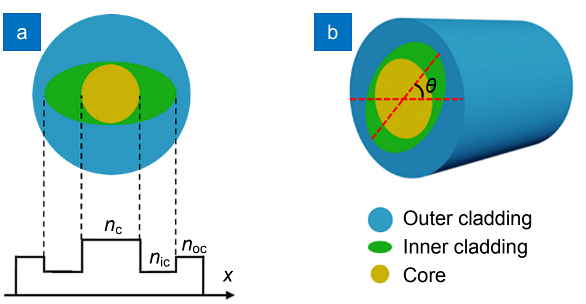

Fig. 3 | (a) Cross section and refractive-index distribution of the IECF. **(b)** Three-dimensional structure of the IECF.

Based on the above analysis, the LP_{01} mode can be converted into the LP_{l1}^c mode by using MSCs. Next, the generation of OAM modes will be discussed. The LP_{l1}^c mode generated by MSCs can be decomposed into two orthogonal degenerate modes LP_{l1}^{θ} (even) and $LP_{l1}^{-\theta}$ (odd). By combining the LP_{l1}^{θ} and $LP_{l1}^{-\theta}$ modes having a phase difference of ±π/2, OAM modes can be generated and expressed as follows[14,17]:

$$OAM_{\pm l1} = LP_{l1}^{\theta} \pm \mathrm{i} \times LP_{l1}^{-\theta} = F_{l1}(r)\exp(\pm il\varphi) . \quad (3)$$

If the phase difference is 0 or π, the combined mode fields can be expressed as follows[14]:

$$LP_{l1}^{\theta} + LP_{l1}^{-\theta} = F_{l1}(r)/\sqrt{2}\cos(l\varphi) \quad \text{or}$$
$$LP_{l1}^{\theta} - LP_{l1}^{-\theta} = F_{l1}(r)/\sqrt{2}\sin(l\varphi) , \quad (4)$$

which represents a 45° rotation of the LP_{l1}^{θ} or $LP_{l1}^{-\theta}$ mode.

When the LP_{l1}^c mode passes through the IECF, n_{eff} will be different between the two orthogonal modes because of the birefringence effect. The difference can be expressed as

$$\Delta n_{eff} = n_{eff}(LP_{l1}^{-\theta}) - n_{eff}(LP_{l1}^{\theta}) . \quad (5)$$

In order to design the proper IECF length (L_{IECF}) for generating different OAM modes, we calculate the Δn_{eff} using COMSOL software and the corresponding beat length (Λ) at a wavelength of 1550 nm, as listed in Table 1, where Λ can be expressed as $\Lambda = \lambda/\Delta n_{eff}$.

Mode converter

The evolution diagrams of intensity and phase from the LP_{01} mode to LP_{l1}^c modes that are decomposed into two degenerate orthogonal modes LP_{l1}^{θ} and $LP_{l1}^{-\theta}$ when the LP_{01} mode passes through the MSCs, and those from two degenerate modes to OAM$_{\pm 11}$, OAM$_{\pm 21}$, and OAM$_{\pm 31}$ modes when LP_{l1}^c modes pass through the IECFs are illustrated in Fig. 4. When the L_{IECF} is set to a quarter beat

Table 1 | Structural parameters of IECFs for the generation of OAM modes

Mode	OAM_{11}/OAM_{-11}	OAM_{21}/OAM_{-21}	OAM_{31}/OAM_{-31}
Δn_{eff}	0.5×10^{-4}	0.8×10^{-4}	0.9×10^{-4}
Λ (mm)	31	19.4	17.22
L_{IECF} (mm)	7.75/23.25	4.84/14.53	4.3/12.9

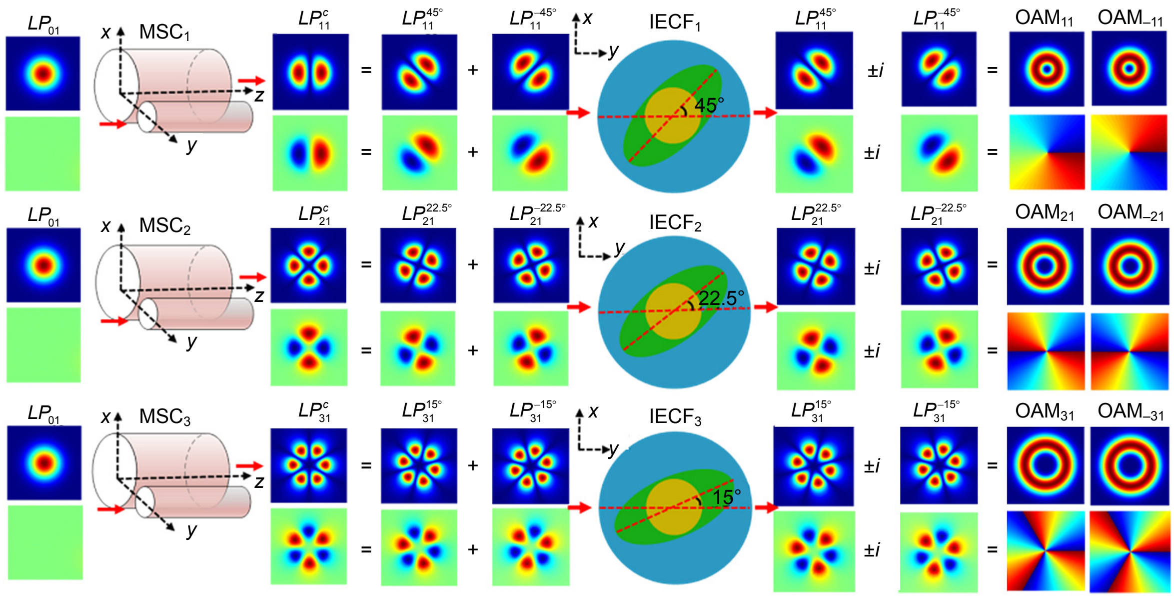

Fig. 4 | Evolution diagrams of intensity and phase from the LP_{01} mode to the LP_{11}^c, LP_{21}^c, and LP_{31}^c modes by coupling in the designed MSCs and those from the LP_{11}^c, LP_{21}^c, and LP_{21}^c modes to the $OAM_{\pm11}$, $OAM_{\pm21}$, and $OAM_{\pm31}$ modes after passing through the designed IECFs with different splicing angles of 45°, 22.5°, and 15°[34].

length ($\Lambda/4$), a π/2 phase difference can be obtained between two degenerate modes, and the OAM_{11}, OAM_{21}, and OAM_{31} modes can be obtained. The IECF should generate not only the positive TCs but also the negative ones. One can change the sign of the TCs by changing the L_{IECF} to obtain a −π/2 phase difference. The L_{IECF} of the designed fiber is set to $3\Lambda/4$ for generating the OAM_{-11}, OAM_{-21}, and OAM_{-31} modes. As the phase difference is π/2 or −π/2 after a propagation distance of $\Lambda/4$ or $3\Lambda/4$ in the IECF, respectively, the fiber length should be odd multiples of $\Lambda/4$. The structural parameters of IECFs for the generation of OAM modes are listed in Table 1. Notably, according to the coupling mode theory, the polarization states of the output LP_{lm} modes are the same as that of the input LP_{01} mode[32,36].

Discussion

We also simulated the normalized power evolution between the LP_{l1}^c modes and LP_{l1}^s modes along the propagation length in the IECF, which is analyzed by using the beam propagation method, as shown in Fig. 5. The IECF can be used as a mode rotator for the conversion between two degenerate LP modes, which is similar to the method in Ref.[37]. The intersection points of each pair of curves are the corresponding positions of generation of $OAM_{\pm l1}$ modes. The propagation lengths are consistent with those listed in Table 1. By appropriately designing the L_{IECF} and controlling the rotation angle θ, one can selectively generate different OAM modes.

Furthermore, the evolutions with different L_{IECF} values are analyzed. The phase difference between odd and even modes varies with L_{IECF}, and the generated optical field can be described as

$$LP_{l1}^{\theta}+\exp(\mathrm{i}\omega)\cdot LP_{l1}^{-\theta}=A_{l1}(r,p,\varphi)\exp[\mathrm{i}\alpha(p,\varphi)]\,, \quad (6)$$

where A_{l1} is the amplitude distribution and α is the phase distribution. These distributions can be expressed as follows:

$$A_{l1}(r,p,\varphi)=F_{l1}(r)\sqrt{1+2\cos(l\varphi)\sin(l\varphi)\cos p}\,,$$
$$\alpha(p,\varphi)=\arctan[\frac{\sin p\sin(l\varphi)}{\cos(l\varphi)+\cos p\sin(l\varphi)}]\,, \quad (7)$$

where $p=2\pi L_{IECF}/\Lambda$ is the phase difference between the odd and even modes. The local helicity of the interference can be expressed as[13]

$$\frac{\partial\alpha(p,\varphi)}{\partial\varphi}=\frac{\sin p}{1+\sin(2l\varphi)\cos p}\,. \quad (8)$$

The average OAM can be continuously varied with respect to p. We choose the generation of the first-order OAM mode as an example. Figures 6(a)~6(d) show the intensity, phase, interference, and local helicity distributions of the OAM mode with $l = \pm 1$ generated by MSC_1 and $IECF_1$ with different values of L_{IECF}, respectively. As shown in the figure, the OAM mode can be generated with different values of L_{IECF}. However, the variations of phase distributions of the generated OAM mode are not uniform, as shown in Fig. 6(b), and the intensities of the OAM mode are weak. We can also observe the spiral arms to determine the TC of the OAM mode in the interference patterns of the generated OAM beam and a reference Gaussian beam, as shown in Fig. 6(c). As shown in Fig. 6(d), the helicity of the generated OAM mode is also not uniform with the change of L_{IECF}, which implies that the generated OAM mode is not pure. To improve the purity, θ should be equal to $\pi/2$ or $3\pi/2$ if possible.

Finally, the OAM intensity spectrum of the generated OAM mode is quantitatively analyzed. As shown in Fig. 7, $|C_l|^2$ represents the energy of the $OAM_{\pm 1}$ component over the total field, i.e., the OAM intensity spectrum or energy spectrum[39,40]. To generate a highly pure OAM mode, ω should be $\pi/2$ or $3\pi/2$ if possible, which implies that L_{IECF} should be 7.75 mm or 23.25 mm. Further, the OAM intensity spectrum is close to 1, which indicates that the OAM mode-conversion efficiency is close to 100%. If L_{LECF} is 0 or 15.5 mm, the coupled mode will be the $LP_{11}^{45^\circ}$ or $LP_{11}^{-45^\circ}$ mode, and the mode intensity spectrum is 50%. Similarly, we can also obtain the properties of OAM modes with $l = \pm 2$ or ± 3, generated by MSC_2 cascaded with $IECF_2$ or MSC_3 cascaded with $IECF_3$, respectively, at different values of L_{LECF}. The purities of OAM modes in these two cases are also nearly 100% when L_{IECF} is simultaneously equal to odd multiples of $\Lambda/4$ for the desired mode and even multiples of $\Lambda/4$ for unwanted modes.

Although the MSC we used above is dependent on wavelength, it is a broadband mode converter with a certain bandwidth, as shown in Fig. 4 in Ref.[34]. One can further expand the response bandwidth of the IECF for matching the MSC by replacing the inner elliptical cladding with tunable functional materials[41].

In Ref.[34,35], the MSC was used to excite lower-order *LP* modes, and the phase shift was achieved using a polarization controller. In contrast to the previous work, we firstly introduce the combination of the IECF with the MSC to generate HO-OAM modes with $l = \pm 1, \pm 2, \pm 3$. By appropriately designing the mode converter and changing the parameters of the fiber for supporting higher modes, OAM modes of even higher orders ($|l|>3$) can

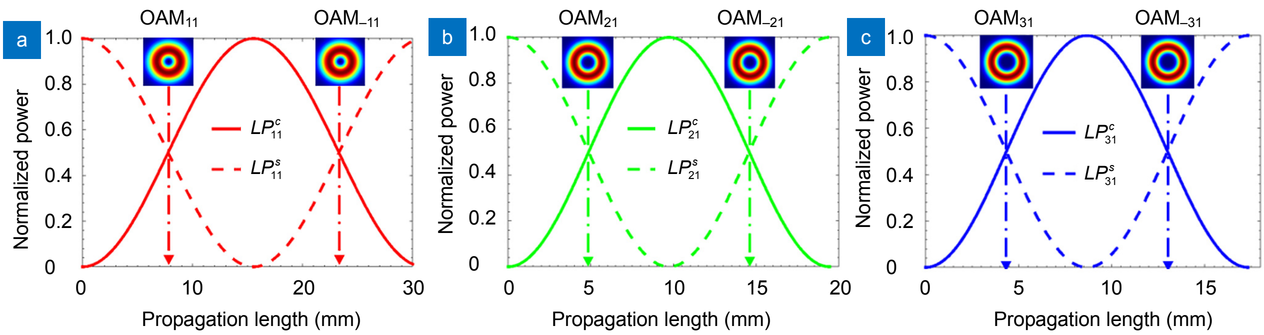

Fig. 5 | Normalized power evolution between the LP_{l1}^c modes and LP_{l1}^s modes along the propagation length of IECFs. The intersection points of each pair of curves are the corresponding positions of generation of $OAM_{\pm l1}$ modes.

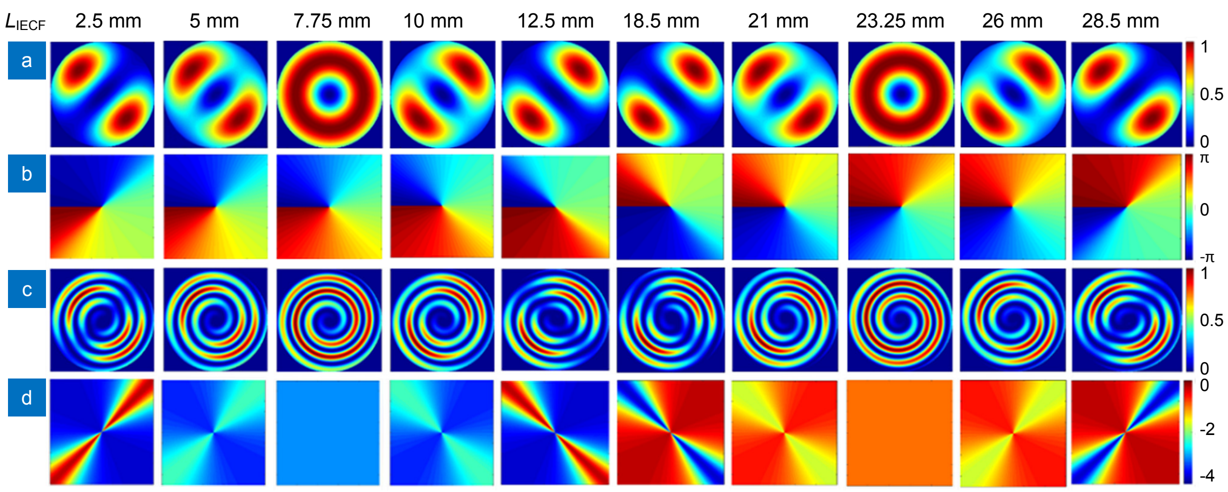

Fig. 6 | Intensity, phase, interference, and local helicity distributions of the OAM mode with TCs of $l = \pm 1$ generated by MSC_1 and $IECF_1$ at different values of L_{IECF}.

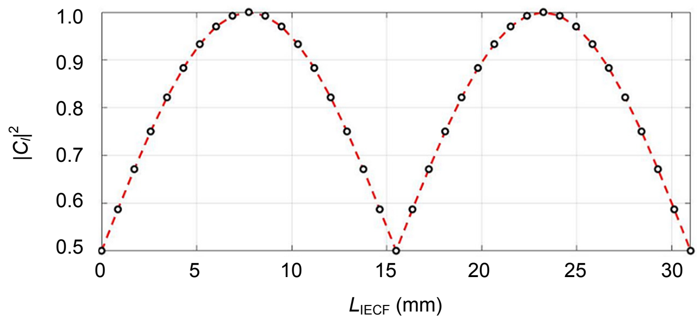

Fig. 7 | Purity of the first-order OAM mode generated by MSC$_1$ cascaded with IECF$_1$ at different values of L_{IECF}.

also be generated. However, it is worth noting that the coupling efficiency decreases with the increase of mode order.

Conclusion

In this work, we designed and simulated an all-fiber-based mode converter composed of an MSC and an IECF to generate OAM modes with TCs ranging from $l = \pm1$ to $l = \pm3$ at a mode-conversion efficiency of almost 100%. First, the MSC is utilized to convert the fundamental mode LP_{01} to LP_{l1}^{c} modes, which can be decomposed into two degenerate orthogonal modes LP_{l1}^{θ} and $LP_{l1}^{-\theta}$. Subsequently, a phase difference of $\pm\pi/2$ between two orthogonal modes can be achieved to convert them to OAM modes after a certain propagation length in the IECF, which is an odd multiple of a quarter beat length. Finally, the OAM modes generated at different lengths of the IECF were quantitatively analyzed. In practice, this OAM mode converter is easy to fabricate with existing optical-fiber drawing techniques and will allow us to take advantage of the increase in transmission capacity and spectral efficiency in an all-fiber communication system based on OAM modes.

References

1. Allen L, Beijersbergen M W, Spreeuw R J C, Woerdman J P. Orbital angular momentum of light and the transformation of Laguerre-Gaussian laser modes. *Phys Rev A* **45**, 8185–8189 (1992).
2. Wang J, Yang J Y, Fazal I M, Ahmed N, Yan Y *et al*. Terabit free-space data transmission employing orbital angular momentum multiplexing. *Nat Photonics* **6**, 488–496 (2012).
3. Willner A E, Huang H, Yan Y, Ren Y, Ahmed N *et al*. Optical communications using orbital angular momentum beams. *Adv Opt Photonics* **7**, 66–106 (2015).
4. Bozinovic N, Yue Y, Ren Y, Tur M, Kristensen P *et al*. Terabit-scale orbital angular momentum mode division multiplexing in fibers. *Science* **340**, 1545–1548 (2013).
5. Dholakia K, Čižmár T. Shaping the future of manipulation. *Nat Photonics* **5**, 335–342 (2011).
6. Padgett M, Bowman R. Tweezers with a twist. *Nat Photonics* **5**, 343–348 (2011).
7. Tkachenko G, Brasselet E. Helicity-dependent three-dimensional optical trapping of chiral microparticles. *Nat Commun* **5**, 4491 (2014).
8. Hell S W, Wichmann J. Breaking the diffraction resolution limit by stimulated emission: stimulated-emission-depletion fluorescence microscopy. *Opt Lett* **19**, 780–782 (1994).
9. Nicolas A, Veissier L, Giner L, Giacobino E, Maxein D *et al*. A quantum memory for orbital angular momentum photonic qubits. *Nat Photonics* **8**, 234–238 (2014).
10. Sueda K, Miyaji G, Miyanaga N, Nakatsuka M. Laguerre-Gaussian beam generated with a multilevel spiral phase plate for high intensity laser pulses. *Opt Express* **12**, 3548–3553 (2004).
11. Beijersbergen M W, Allen L, Van der Veen H E L O, Woerdman J P. Astigmatic laser mode converters and transfer of orbital angular momentum. *Opt Commun* **96**, 123–132 (1993).
12. Dashti P Z, Alhassen F, Lee H P. Observation of orbital angular momentum transfer between acoustic and optical vortices in optical fiber. *Phys Rev Lett* **96**, 043604 (2006).
13. Jiang Y C, Ren G B, Lian Y D, Zhu B F, Jin W X *et al*. Tunable orbital angular momentum generation in optical fibers. *Opt Lett* **41**, 3535–3538 (2016).
14. Li S H, Mo Q, Hu X, Du C, Wang J. Controllable all-fiber orbital angular momentum mode converter. *Opt Lett* **40**, 4376–4379 (2015).
15. Chen R S, Sun F L, Yao J N, Wang J H, Ming H *et al*. Mode-locked all-fiber laser generating optical vortex pulses with tunable repetition rate. *Appl Phys Lett* **112**, 261103 (2018).
16. Jin X Q, Pang F F, Zhang Y, Huang S J, Li Y C *et al*. Generation of the first-order OAM modes in single-ring fibers by offset splicing technology. *IEEE Photonic Tech L* **28**, 1581–1584 (2016).
17. Zhang Y, Pang F F, Liu H H, Jin X Q, Huang S J *et al*. Generation of the first-order OAM modes in ring fibers by exerting pressure technology. *IEEE Photonics J* **9**, 7101609 (2017).
18. Lin Z X, Wang A T, Xu L X, Zhang X Q, Sun B *et al*. Generation of optical vortices using a helical fiber Bragg grating. *J Lightwave Technol* **32**, 2152–2156 (2014).
19. Zhang X Q, Wang A T, Chen R S, Zhou Y, Ming H *et al*. Generation and conversion of higher order optical vortices in optical fiber with helical fiber Bragg gratings. *J Lightwave Technol* **34**, 2413–2418 (2016).
20. Fang L, Wang J. Flexible generation/conversion/exchange of fiber-guided orbital angular momentum modes using helical gratings. *Opt Lett* **40**, 4010–4013 (2015).
21. Fang L, Wang J. Mode conversion and orbital angular momentum transfer among multiple modes by helical gratings. *IEEE J Quantum Elect* **52**, 6600306 (2016).
22. Yan Y, Wang J, Zhang L, Yang J Y, Fazal I M *et al*. Fiber coupler for generating orbital angular momentum modes. *Opt Lett* **36**, 4269–4271 (2011).
23. Yan Y, Zhang L, Wang J, Yang J Y, Fazal I M *et al*. Fiber struc-

ture to convert a Gaussian beam to higher-order optical orbital angular momentum modes. *Opt Lett* **37**, 3294–3296 (2012).
24. Huang W, Liu Y G, Wang Z, Zhang W C, Luo M M *et al*. Generation and excitation of different orbital angular momentum states in a tunable microstructure optical fiber. *Opt Express* **23**, 33741–33752 (2015).
25. Guan B B, Scott R P, Qin C, Fontaine N K, Su T H *et al*. Free-space coherent optical communication with orbital angular, momentum multiplexing/demultiplexing using a hybrid 3D photonic integrated circuit. *Opt Express* **22**, 145–156 (2014).
26. Su T H, Scott R P, Djordjevic S S, Fontaine N K, Geisler D J *et al*. Demonstration of free space coherent optical communication using integrated silicon photonic orbital angular momentum devices. *Opt Express* **20**, 9396–9402 (2012).
27. Fontaine N K, Doerr C R, Buhl L L. Efficient multiplexing and demultiplexing of free-space orbital angular momentum using photonic integrated circuits. In *OFC/NFOEC* 1–3 (IEEE, 2012).
28. Cai X L, Wang J W, Strain M J, Johnson-Morris B, Zhu J B *et al*. Integrated compact optical vortex beam emitters. *Science* **338**, 363–366 (2012).
29. Ren H R, Li X P, Zhang Q M, Gu M. On-chip noninterference angular momentum multiplexing of broadband light. *Science* **352**, 805–809 (2016).
30. Wang S, Deng Z L, Cao Y Y, Hu D J, Xu Y *et al*. Angular momentum-dependent transmission of circularly polarized vortex beams through a plasmonic coaxial nanoring. *IEEE Photonics J* **10**, 5700109 (2018).
31. Pu M B, Li X, Ma X L, Wang Y Q, Zhao Z Y *et al*. Catenary optics for achromatic generation of perfect optical angular momentum. *Sci Adv* **1**, e1500396 (2015).
32. Riesen N, Love J D. Weakly-guiding mode-selective fiber couplers. *IEEE J Quantum Elect* **48**, 941–945 (2012).
33. Whalen M S, Wood T H. Effectively nonreciprocal evanescent-wave optical-fibre directional coupler. *Electron Lett* **21**, 175–176 (1985).
34. Wang T, Wang F, Shi F, Pang F F, Huang S J *et al*. Generation of femtosecond optical vortex beams in all-fiber mode-locked fiber laser using mode selective coupler. *J Lightwave Technol* **35**, 2161–2166 (2017).
35. Wan H D, Wang J, Zhang Z X, Cai Y, Sun B *et al*. High efficiency mode-locked, cylindrical vector beam fiber laser based on a mode selective coupler. *Opt Express* **25**, 11444–11451 (2017).
36. Huang W P. Coupled-mode theory for optical waveguides: an overview. *J Opt Soc Am A* **11**, 963–983 (1994).
37. Zeng X L, Li Y, Li W, Zhang L Y, Wu J. All-fiber broadband degenerate mode rotator for mode-division multiplexing systems. *IEEE Photonic Tech L* **28**, 1383–1386 (2016).
38. Katsuyama T, Matsumura H, Suganuma T. Low-loss single-polarization fibers. *Electronics Lett* **17**, 473–474 (1981).
39. Molina-Terriza G, Torres J P, Torner L. Management of the angular momentum of light: preparation of photons in multidimensional vector states of angular momentum. *Phys Rev Lett* **88**, 013601 (2001).
40. Zhao P, Li S K, Feng X, Cui K Y, Liu F *et al*. Measuring the complex orbital angular momentum spectrum of light with a mode-matching method. *Opt Lett* **42**, 1080–1083 (2017).
41. Han Y, Liu Y G, Huang W, Wang Z, Guo J Q *et al*. Generation of linearly polarized orbital angular momentum modes in a side-hole ring fiber with tunable topology numbers. *Opt Express* **24**, 17272–17284 (2016).

Acknowledgements
This work was supported by National Natural Science Foundation of China (Grant No. 61275049).

Competing interests
The authors declare no competing financial interests.